archives
of thermodynamics
Vol. **41**(2020), No. 2, 3–34
DOI: 10.24425/ather.2020.132958

Heat transfer and friction factor correlation for inclined spherical ball roughened solar air heater

RAMESH MURMU*
PARMANAND KUMAR
HARI N. SINGH

National Institute of Technology, Department of Mechanical Engineering, Adityapur, Jamshedpur, Jharkhand 831014, India

Abstract Flow mechanism under roughened solar air heater is quite complex. This paper is an effort towards determining the governing equations for heat transfer and friction factor for inclined spherical balls roughened ducts. With the availability of these equations, it is easier to predict the thermal and thermohydraulic performance of such roughened solar air heaters. The governing equations are derived based on the experimental data generated under actual outdoor condition at the test rig designed and fabricated at the terrace of the Mechanical Engineering Department, the National Institute of Technology Jamshedpur in India, in terms of roughness and flow parameters. Maximum augmentation in Nusselt number and friction factor for varying relative roughness pitch, relative roughness height, spherical ball height to diameter ratio, and angle of attack was respectively found to be of the order of 2.1 to 3.54 times, 1.87 to 3.21 times, 2.89 to 3.27 times and 1.74 to 3.56 times for Nusselt number and 0.84 to 1.79 times, 1.46 to 1.91 times, 1.67 to 2.34 times and 1.21 to 2.67 times for friction factor in comparison to non-roughened duct. The optimum roughness parameters under present investigation have been found.

Keywords: Renewable energy; Spherical ball, Relative roughness pitch, Relative roughness height; Nusselt number; Friction factor; Angle of attack

*Corresponding Author: Email: murmunitjsr@gmail.com

Nomenclature

A_p	–	surface area of absorber plate, m^2
A_o	–	area of orifice of orifice plate, m^2
C_d	–	coefficient of discharge
C_p	–	specific heat capacity of air, J/kgK
D	–	diameter of orifice, mm
D_h	–	hydraulic diameter of duct, mm
d_b	–	diameter of spherical ball, mm
e	–	roughness or ball's height, mm
g	–	acceleration due to gravity, m/s^2
I	–	intensity of global solar radiation (insolation), W/m^2
H	–	height of SAH duct, m
k	–	thermal conductivity of air, W/mK
L	–	length of SAH duct, m
$\dot{m}$	–	mass flow rate of air, kg/s
ΔP_d	–	test section pressure drop, N/m^2
ΔP_o	–	orifice meter pressure drop, N/m^2
p	–	roughness pitch, mm
Q_u	–	useful heat gain, W
ΔT	–	rise in air temperature, °C
T_o	–	outlet air temperature, °C
T_i	–	air inlet temperature, °C
T_o	–	ambient temperature, °C
T_{pm}	–	mean absorber plate temperature, °C
T_{fm}	–	mean air temperature in the duct, °C
W	–	width of SAH duct, m
W_V	–	wind velocity, m/s
V	–	average velocity of air through the duct, m/s

Greek symbols

α	–	angle of attack, deg
$\alpha/55$	–	relative angle of attack, deg
β	–	ratio of orifice diameter (D_2) to pipe internal diameter (D_1)
μ	–	dynamic viscosity of air, Ns/m^2
ν	–	kinematic viscosity of air, m^2/s
ρ	–	air density, kg/m^3
ρ_m	–	density of manometric fluid (water), kg/m^3

Subscripts

r	–	roughened
s	–	smooth
i	–	inlet
o	–	outlet
f	–	fluid
a	–	air
p	–	plate

Dimensionless parameters

p/e	–	relative roughness pitch
e/D_h	–	relative roughness height
e/d_b	–	pherical ball height to diameter ratio
f	–	friction factor
f_s	–	friction factor for smooth surface
f_r	–	friction factor for roughened duct
Nu	–	Nusselt number
Nu_r	–	Nusselt number for roughened duct
Re	–	Reynolds number
W/H	–	aspect ratio of collector duct

Abbreviations

SAH	–	solar air heater

1 Introduction

Renewable energy is energy that is collected from renewable resources, which are naturally replenished on a human timescale, such as sunlight, wind, rain, tides, waves, and geothermal heat. Renewable energy provides energy in four important areas: electricity generation, air and water heating/cooling, transportation, and rural (off-grid) energy services [1]. Frequent rise in energy prices have motivated many researchers to shift their thrust towards renewable sources of energy. Artificially roughened solar air heater (SAH) is an effective method to use solar heat energy to heat air to be used for many domestic and industrial applications. The solar energy available in a single year exceeds the possible energy output of all of the fossil fuel energy reserves in India. A solar collector is a type of heat exchanger which transfers the radiant energy of the incident sunlight to the sensible heat of a working fluid; air or liquid. Solar collectors absorb the whole spectrum of solar radiation not only the sunlight irrespective of their frequency and wavelength. Solar radiation absorbed by collector includes short wave short radiation and excludes the infrared long radiation ranging from 0.78–3 μm. The quantity of solar energy striking the Earth's surface (solar constant) averages about 1000 W/m^2 under clear skies, depending upon weather conditions, location and orientation. Different types of solar collectors have been designed and developed in the last few years as a result of increased utilization of solar energy [2–4]. Solar air heaters follow a solar thermal technology in which the energy from the sun is captured by an absorbing medium and used to heat air. Solar air heating is a renewable

energy heating technology used to heat or condition air for buildings or process heat applications. It is typically the most cost-effective out of all the solar technologies, especially in commercial and industrial applications, and it addresses the largest usage of building energy in heating climates, which is space heating and industrial process heating [5–7]. The value of heat transfer coefficient and heat capacity for air is low which reduces the heat transfer rate and thus increases the heat loss to the surroundings. A large number of researchers have used solar air heaters of different configurations to remove these drawbacks associated with solar air heaters to better serve the purpose of air heating. Using artificial roughness of various geometry and orientation has been proven to be the most effective method to harness solar energy [8–11]. Han *et al.* [12] investigated the effect of rib pitch to height ratio and rib height to equivalent hydraulic diameter on friction factor and heat transfer coefficient for Reynolds number range of 7000 to 90 000, relative roughness pitch range of 10 to 40 and relative roughness height range of 0.021 to 0.063 and found that the maximum values of friction factor and the Stanton number occur at a relative roughness pitch of 10. Saini and Saini [13] experimentally investigated the effect of arc shaped ribs on the Nusselt number (Nu) and the friction factor (f) of rectangular ducts of solar air heaters. Enhancement of the Nusselt number and friction factor was reported as 3.6 and 1.75 times, respectively, over the smooth surface. The correlations for Nusselt number and friction factor were also developed. Lau *et al.* [14] continued their comparison studies on full and staggered discrete ribs arrays and reported that for a constant pumping power, 60° and 45° discrete ribs enhance the ribbed wall heat transfer by about 5 to 19% and 11 to 32%, respectively, compared to the corresponding full ribs case. Karwa *et al.* [15] carried out an experimental investigation on the integral transverse chamfered rib roughened absorber plate and found two-fold increase in the Stanton number and three-fold increase in the friction factor as compared to that of a smooth duct. Chang *et al.* [16] investigated experimentally the effect of V-shaped ribs and deepened scales and found that the heat transfer enhancement ratios were 9.5–13.6 and 9–12.3 with forward and backward flows respectively for laminar flows and 6.8–6.3 and 5.7–4.3 for turbulent flows. Mahmood *et al.* [17] studied 45° angled rib turbulators and found that the thermal performance is lower in the ribbed channel than in channel with dimples and/or protrusions mostly because of higher rib produced more drag and friction. Ridouane and Campo [18] investigated computationally the heat transfer and pressure drop of laminar air flow in

a parallel-plate channel with transverse hemi-cylindrical cavities and found enhancement in heat transfer by 30% relative to smooth duct and pressure loss increments by 19%. Chandra *et al.* [19] carried out investigation of the heat transfer and friction behavior of a square duct with transverse ribs roughness on one, two, three, and four walls of the duct. The flow Reynolds number was varied from 10 000 to 80 000, relative roughness height (e/D_h) of 0.0625 and the relative roughness pitch (p/e) of 8. They found that the heat transfer is enhanced with the increase in a number of ribbed walls in the channel from 2.16 for one ribbed wall case to 2.57 for four ribbed wall case at the Reynolds number of 30 000. Gupta *et al.* [20,21] investigated 90° continuous, 60° broken ribs and 90° saw tooth profiled and established that the mean heat transfer for square channel with 60° V-broken ribs are more eminent than that of 90° saw tooth profiled rib and 90° continuous ribs. Momin *et al.* [22] investigated the heat transfer and friction characteristics of duct roughened with V-shaped rib roughness with relative roughness height range ftom 0.02 to 0.034, angle of attack range of 30°–90° and Reynolds number in the range from‘ 2500 to 18 000. Relative roughness pitch was kept constant as 10. The maximum enhancement in the heat transfer and friction factor as a result of providing artificial roughness was observed as 2.30 and 2.83 times of that of smooth duct for an angle of attack of 60°. Saini and Saini [23] used expanded metal mesh as artificial roughness at the absorber plate of solar air heater which gave the maximum enhancement in Nusselt number and friction factor of the order of 4 and 5, respectively, and maximum enhancement in thermal efficiency was found as 37–57%. Varun *et al.* [24] experimentally investigated heat transfer and friction characteristics of solar air heater by using a combination of inclined and transverse ribs on the absorber plate of rectangular duct. For relative roughness pitch (p/e) value of 8, the best thermal performance has been obtained. Correlations for Nusselt number and friction factor were also developed. Wongcharee *et al.* [25] investigated the effects of different shaped ribs (rectangular, triangular, cylindrical, concave-concave, convex-concave, long convex-short concave, and long convex-short concave) on heat transfer and friction factor and found that the cylindrical ribs provided the highest value of thermohydraulic performance and minimum enhancement in Nusselt number in case of rectangular ribs. Sethi *et al.* [26] experimentally investigated the effect of artificial roughness on heat transfer and friction characteristics in solar air heater duct having dimple shaped elements arranged in angular arc pattern. The maximum Nusselt number was found

corresponding to relative roughness height of 0.036, relative roughness pitch of 10 and arc angle of 60°. Skullong and Promvonge [27] performed experimental study on the heat transfer and flow friction characteristics in a solar air heater channel fitted with delta-winglet type vortex generators (DWs). The experimental results revealed that in the first case, the 60° DW-E (DW mounted only at the entrance) at roughness pitch of 1 provided highest heat transfer and friction factor while the 30° DW-E performed overall better than the others. Pandey *et al.* [28] studied heat transfer and friction factor in rectangular channel with multiple-arc shaped with gaps as roughness element. The maximum increment in Nusselt number and friction factor was 5.85 and 4.96 times compared to a smooth duct. Kumar *et al.* [29–31] used three sides instead of one side roughened duct and found that augmentation in Nusselt number and friction factor of three sides over one side roughened duct was 21–86 % and 11–41%, respectively. They also reported augmentation in thermal efficiency of three sides over those of one side roughened duct to be 44–56% for varying relative roughness pitch (p/e), and 39–51% for varying relative roughness height (e/D_h). The literature of artificially roughened SAH reveals that considerable amount of experimental and analytical work has been done to investigate the effect of turbulence promoters on Nusselt number and friction factor characteristics of roughened flow passages. Extensive experimentations have been carried out in part, employing artificial roughness *viz.* transverse rib, angled rib, inclined rib with gap, V-shaped rib, discrete or broken V-shaped rib, discrete V-shaped rib with pieces, W-shaped rib, wedge or chamfered shaped rib, dimpled shaped rib, rib-groove, Multi V-shaped rib and Z-shaped rib, for heat transfer enhancement in rectangular ducts. Roughness geometry, irrespective of their shape and size were mostly aligned either normal or inclined to the flow. Regular and discrete roughness geometry and their impact on heat transfer and flow characteristics have already been studied. Rise in heat transfer was obtained but the rise in friction factor was also very high. However no study has been reported on SAH roughened with inclined spherical ball of different height and diameter soldered upon collector's face. Such geometry would facilitate more formation of secondary flow, i.e., flow of heated air in contact of roughness element leading to increase in useful heat gain of air and reduction in propelling power input due to gaps between spherical balls of relevant pitch, height and diameter. Hence, with an expectation that more improvement in local heat transfer and rise in useful heat gain under inclined spherical ball roughened SAH can be obtained as such ge-

ometry and orientation can increase the number of secondary flow stream due to variation in angle of attack and geometrical dimension, the present research has been taken up with an objective to determine the rise in Nusselt number and friction factor for roughened duct over smooth duct by conducting experimentation under actual outdoor condition, to determine the optimum roughness parameters that yields maximum Nusselt number at minimum friction factor and to establish correlations for Nusselt number and friction factor in terms of flow and operating parameters.

2 Experiments

Investigation is conducted to obtain the experimental values of the Nusselt number ($\mathrm{Nu}_{r)}$ and the friction factor (f_r) for spherical ball roughened collectors. The test rig was fabricated and calibrated properly before taking data for roughened and non-roughened ducts. The test rig had two ducts capable of accommodating roughened and non-roughened ducts simultaneously. The various sets of data recorded from the test rig included: inlet and outlet air temperatures, plate temperatures, pressure drop across the duct and the orifice and solar insolation.

2.1 Test rig

The experimental set-up has been designed and fabricated as per the ASHRAE standards [32]. Figures 1 and 2 show the schematic and actual photograph of experimental set-up. The rectangular duct having dimensions 2150 mm × 330 mm × 30 mm in which test length is 1200 mm and lengths of entry and exit sections are 650 mm and 300 mm, respectively. The aspect ratio (W/H, where W is the width and H is the height) of the duct is 11. The entry section is made in a bell-mouthed shape at the inlet side to avoid loses at the entry. A control valve is provided to control the flow in both ducts. Calibrated orifice meter is installed to measure the flow rate of air through the roughened ducts. A copper constantan thermocouple has been provided at various locations to measure the plate temperatures. A digital pyranometer system was used to measure solar radiation, wind velocity, ambient temperatures. Figures 3 and 4 show the actual and schematic diagram of the spherical ball roughened plate used under present study. Figure 5 shows the schematic diagram of roughened and non-roughened ducts. Figure 6 shows the positioning of thermocouples and

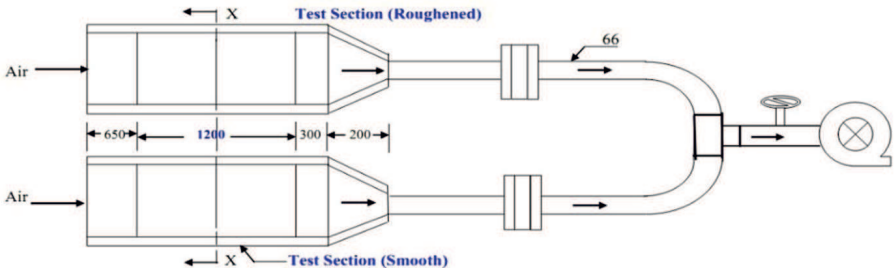

Figure 1: Schematics of test rig.

Figure 2: Photograph of test-rig.

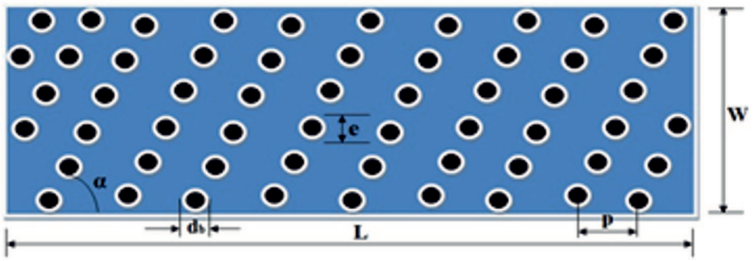

Figure 3: Schematics of spherical ball roughened absorber.

digital thermometers for measuring absorber's surface and air temperature respectively. Photograph of digital pyranometer system has been shown in Fig 7.

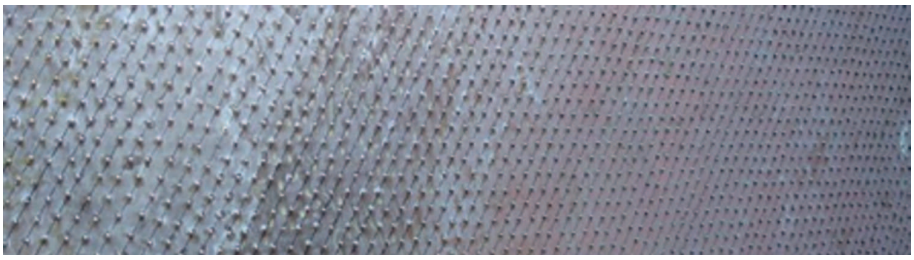

Figure 4: Photograph of spherical ball roughened absorber.

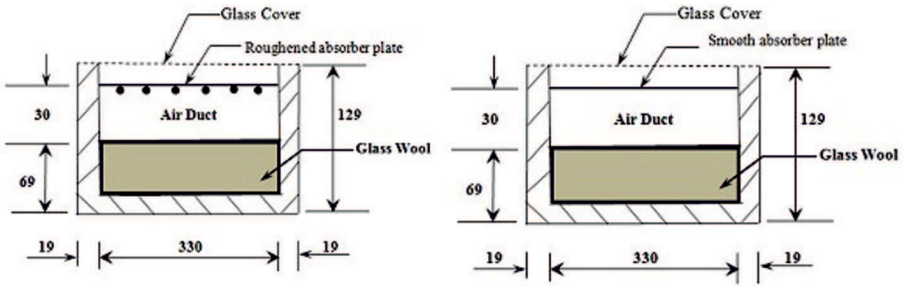

Figure 5: Schematics of roughened and non-roughened ducts.

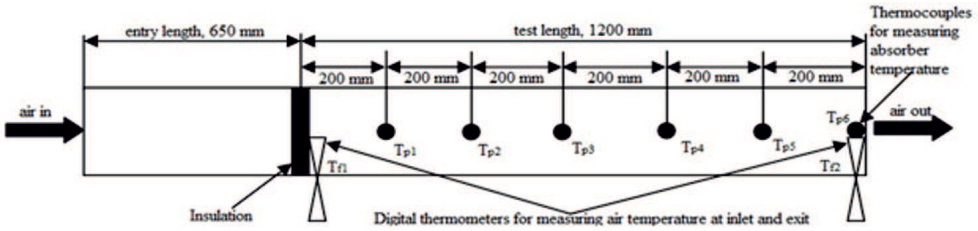

Figure 6: Positioning of thermocouples and digital thermometers.

2.2 Roughness parameters range

SAH roughened passage has a length $L = 1200$ mm, hight $H = 30$ mm, and width $W = 300$ mm, and the hydraulic diameter, $D_h = 54.54$ mm. The spherical ball roughness geometry has been provided under various sets of dimensionless parameters under varying relative roughness pitch (p/e, where p is the roughness pitch and e is the roughness height) 9–18, relative roughness height (e/D_h) 0.024-0.040, ball height to diameter ratio (e/d_b) 0.5–2 and relative angle of attack ($\alpha/55$) 35°–75°. The flow

Figure 7: Photograph of digital pyranometer system.

Reynolds number has been varied from 2500 to 18 500 to generate the best result in terms of the Nusselt number (Nu_r) and friction factor (f_r) for roughened duct. Table 1 shows the range of experimental set-up and operating roughness parameters.

Table 1: Details of experimental set-up and operating conditions.

No.	Parameter		Values/Range	Units
1	Duct parameters	Entry length	650	mm
		Test section length (L)	1200	mm
		Exit length	300	mm
		Width (W)	330	mm
		Height (H)	30	mm
		Duct aspect ratio (W/H)	11	mm
		Hydraulic diameter (D_h)	54.54	mm
		Glass cover thickness (t_g)	4	mm
		Distance between top glass cover and absorber plate (L_1)	30	mm
2	Roughness parameters	Relative roughness pitch (p/e)	9–18	–
		Relative roughness height (e/D_h)	0.024-0.040	–
		Ball height to diameter ratio (e/d_b)	0.5–2	–
		Angle of attack (α)	35–75	degree
3	Flow parameters	Mass flow rate ($\dot{m}$)	0.0104–0.05126	kg/s
		Reynolds number (Re)	2500–18500	–
4	Experimental conditions	Ambient temperature (T_a)	21–41	°C
		Solar radiation	674–986	$\mathrm{W/m^2}$
		Wind velocity (W_v)	0.7–3.1	m/s

The values/range of geometrical parameters of solar air heater duct, roughness parameters and experimental conditions, e.g., mass flow rate, wind velocity, etc. used during experimentation have been given in Tab. 1.

2.3 Data reduction

The mean temperatures, T_{pm} (mean absorber plate temperature) and T_{fm} (mean air temperature in the duct) are simply the arithmetic mean of the noted values of temperatures at different locations between inlet and exit of test section:

$$T_{pm_r} = \frac{T_{p1} + T_{p2} + ... + T_{p6}}{6} , \tag{1}$$

$$T_{fm_r} = \frac{T_{f1} + T_{f6}}{2} . \tag{2}$$

Mass flow rate measurement

Using the pressure drop measurement across the orifice (Δp_0), the flow rate of air under roughened plate is calculated as

$$\dot{m} = C_d A_o \left[\frac{2\rho \Delta p_o}{1-\beta^4}\right]^{0.5} . \tag{3}$$

Friction factor

The friction factor value is calculated using pressure drop (Δp_d), across the test section length (L) of 1200 mm and the mass flow rate ($\dot{m}$) as

$$f = \frac{\triangle\, p_d D_h}{2\rho L v_d^2} , \tag{4}$$

where D_h is the hydraulic diameter for the duct and is evaluated as

$$D_h = \frac{4WH}{[2(W+H)]} \tag{5}$$

and v_d is the flow velocity of air flowing inside the roughened duct.

Reynolds number

The Reynolds number Re is calculated using

$$\mathrm{Re} = \frac{v_d D_h}{\upsilon} . \tag{6}$$

Heat transfer coefficient

Useful heat gain of air is given by

$$Q_u = \dot{m} C_p \left(T_6 - T_1\right) \ . \tag{7}$$

The heat transfer coefficient for the heated test section has been calculated from

$$h = \frac{Q_u}{A_p \left(T_{pm} - T_{fm}\right)} \ , \tag{8}$$

where A_p is the heat transfer area, assumed corresponding one side roughened plate area.

Nusselt number

The heat transfer coefficient is used to determine the Nusselt number and is determined as

$$\mathrm{Nu} = \frac{hD_h}{k} \ , \tag{9}$$

where k is the thermal conductivity of the air.

2.4 Validation of experimental data

Alongside roughened ducts, data were also recorded for non-roughened duct for validating the experimental set-up. The data of the Nusselt number and friction factor obtained from experimentation have been compared with those of data obtained from the correlation.

For non-roughened surface Nu_s as per Dittus-Boelter equation is given by

$$\mathrm{Nu}_s = 0.023 \mathrm{Re}^{0.8} \mathrm{Pr}^{0.4} \tag{10}$$

and f_s for non-roughened surface as per modified Blasius equation is given by

$$f_s = 0.085 \mathrm{Re}^{-0.25} \ , \tag{11}$$

where the subscript s denotes the smooth surface.

The data for the Nusselt number and friction factor of non-roughened ducts so obtained from experimentation and the correlations suggested above compared well with a mean deviation in experimental and estimated values, as ± 3.5 % for Nu_s and $\pm$ 4.4 % for f_s. Figure 8 indicates the comparison of experimental values of the Nusselt number and friction factor with those obtained from the correlations (10) and (11).

2.5 Uncertainty analysis

Irrespective of the extent of precautions taken while recording the experimental data, calibrating all the apparatus used in experimental set-up and discarding the arbitrary readings, there exists a possibility of uncertainty in the measurement of various parameters. Based on the method of Kline and McClintock [33] of the uncertainties associated with various parameters, the uncertainties have been determined. Uncertainty values of various parameters are presented in Tab. 2.

Table 2: Uncertainties in measurement of various parameters.

No.	Name of parameter	Uncertainty range (%)
1.	Area of absorber plate (A_p)	0.080
2.	Cross sectional area of air flow duct (A_c)	0.160
3.	Area of orifice meter (A_o)	0.260
4.	Hydraulic diameter	0.370
5.	Density	0.106
6.	Mass flow rate	0.840
7.	Velocity of air through test section	0.760
8.	Reynolds Number (Re)	0.800
9.	Heat transfer coefficient	3.724
10.	Nusselt number (Nu)	4.357
11.	Friction factor (f)	4.871
12.	Useful heat gain	3.753

3 Results and discussions

Effects of providing spherical ball roughness element inclined to flow has been visualized and discussed. The present investigation is aimed at examining how the Nusselt number and friction factor are affected by spherical ball roughness element and their varying roughness parameters. The literature reveals that introducing roughness on absorber's surface enhances heat transfer coefficient but the matter of concern is that it also increases frictional losses; consequently pumping power required to propel air inside roughened duct increases which results in higher power consumption, thereby reducing collector's performance. Thus, roughness parameters should be selected such that maximum heat transfer is obtained at

minimum rise in pressure drop. This can only be achieved if the Nusselt number (Nu_r) and friction factor and (f_r) characteristics of the roughened duct are known.

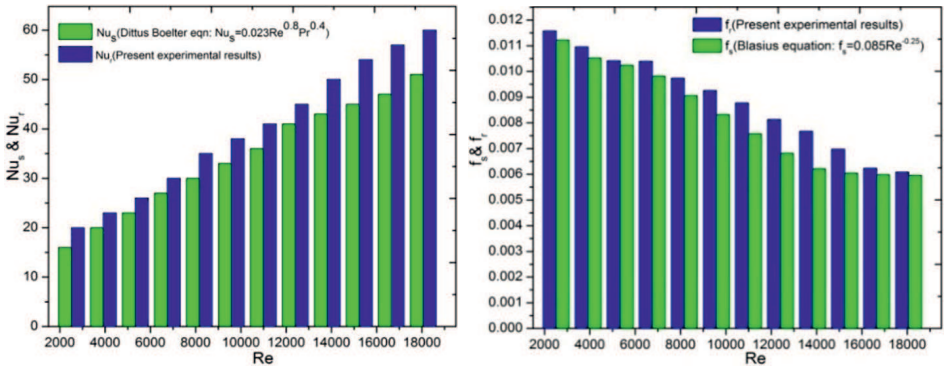

(a) Nusselt number (Nu_s) for smooth duct (b) Friction factor (f_s) for smooth duct

Figure 8: Comparison between experimental and calculated values of the Nusselt number and friction factor for inclined spherical ball roughened solar air heater.

Under present experimental investigation, effects of spherical ball roughness element parameters such as: the relative roughness pitch (p/e) and height (e/D_h), the ball height to diameter ratio (e/d_b), angle of attack (α) on the Nusselt number and friction factor have been studied exhaustively and presented as rise in Nu_r and f_r with mass flow rate of air (Reynolds number). To visualize the effects of roughness parameters, Nu_r and f_r is plotted against these parameters at some selected values of Reynolds number. Correlations for the Nusselt number and friction factor have been derived in terms of roughness and flow parameters in the parametric range investigated.

3.1 Correlations for the Nusselt number and friction factor

Experimental data suggests that the Nusselt number and friction factor are strongly dependent upon system and operating parameters. Functional relationship for Nu_r and f_r can be written as:

$$\mathrm{Nu}_r = f(\mathrm{Re}, p/e, e/D_h, e/d_b, \alpha/55), \tag{12}$$

$$f_r = f(\mathrm{Re}, p/e, e/D_h, e/d_b, \alpha/55)\ . \tag{13}$$

To obtain the performance of spherical ball roughened SAH duct, the Nusselt number and friction factor correlation are developed between dependent variable (Nu_r and f_r) and independent variable: flow and geometrical parameters (Re, p/e, e/D_h, e/d_b , and α).

3.2 Nusselt number correlation

Roughness geometry and flow parameters have the following effects on Nu_r:

- Nu_r increases monotonically with an increase in Re.
- Nu_r varies with the varying p/e and attains maximum value at $p/e = 15$.
- Nu_r varies with the varying e/D_h and attains maximum value at $e/D_h = 0.036$.
- Nu_r varies with the variation in depth to diameter ratio e/d_b and attains maximum value at $e/d = 1$.
- Nu_r varies with the variation in α and attains maximum value at $\alpha = 35°$.

Regression analysis of experimental data was done to obtain the best fit curve and determine statistical correlations for Nusselt number. Firstly, a functional relationship between Nu_r and Re is obtained by plotting ln (Nu_r) and ln (Re) for all the data points as depicted in Fig. 9. To fit a straight line through these points using regression analysis, equation of the line can be written as:

$$\mathrm{Nu} = A_0 \mathrm{Re}^{1.0459} , \tag{14}$$

where A_0 is a function of other parameters, i.e. e/D_h.

For visualizing effects of e/D_h, the values of $\mathrm{Nu}/\mathrm{Re}^{1.0459}$ ($\mathrm{Nu}/\mathrm{Re}^{1.0459}$) are computed using experimental data of Nu_r obtained at constant values other roughness parameters. These values have been plotted against respective e/D_h values as depicted in Fig. 10. Regression analysis for fitting 2nd order quadratic curve represented by following expression:

$$\ln\left(\frac{\mathrm{Nu}}{\mathrm{Re}^{1.0459}}\right) = \ln A_0 + A_1 \ln\frac{e}{D_h} + A_2\left(\ln\frac{e}{D_h}\right)^2 . \tag{15}$$

From the first order regression of the data, the value of slope (m) is obtained as 2.8326. By putting the value of slope in Eq. (15), following correlation

has been obtained:

$$\frac{\mathrm{Nu}}{\mathrm{Re}^{1.0459}} \; A_0 \left(\frac{e}{D_h} \right)^{2.8326} \exp\left(-0.87\right) \left(\ln \frac{e}{D_h} \right)^2 . \tag{16}$$

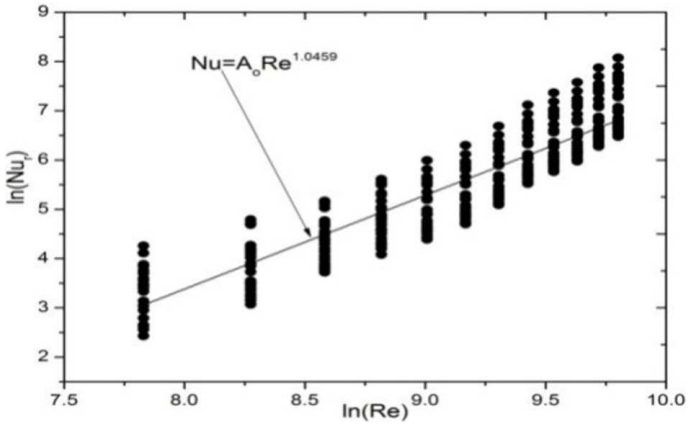

Figure 9: Linear fit curve for $\ln \mathrm{Nu}_r$ *vs.* $\ln \mathrm{Re}$.

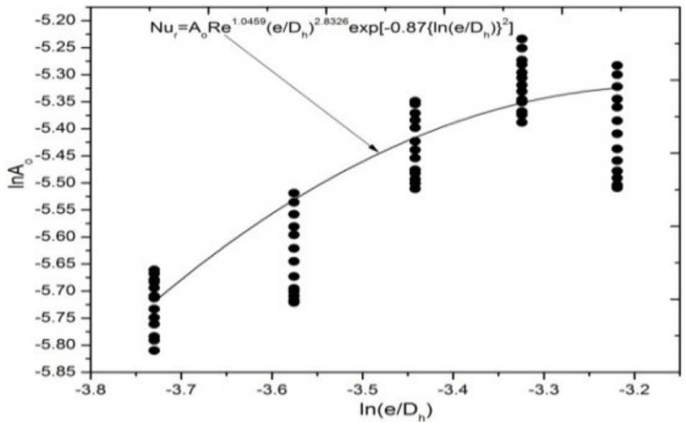

Figure 10: Plot of $\ln A_0$ *vs.* $\ln(e/D_h)$.

The constant A_0 will be a function of p/e. In order to introduce the effect of p/e, the expression

$$\frac{\mathrm{Nu}}{\mathrm{Re}^{1.0459}} \left(\frac{e}{D_h} \right)^{2.8326} \exp\left(-0.87\right) \left(\ln \frac{e}{D_h} \right)^2$$

has been computed from experimental data of Nusselt number obtained at constant values of other roughness parameters. These values are plotted against respective p/e values as depicted in Fig. 11, where

$$B_0 = \frac{\frac{\mathrm{Nu}}{\mathrm{Re}^{1.0459}}}{\left(\frac{e}{D_h}\right)^{2.8326} \exp\left(-0.87\right) \left(\ln\frac{e}{D_h}\right)^2}. \tag{17}$$

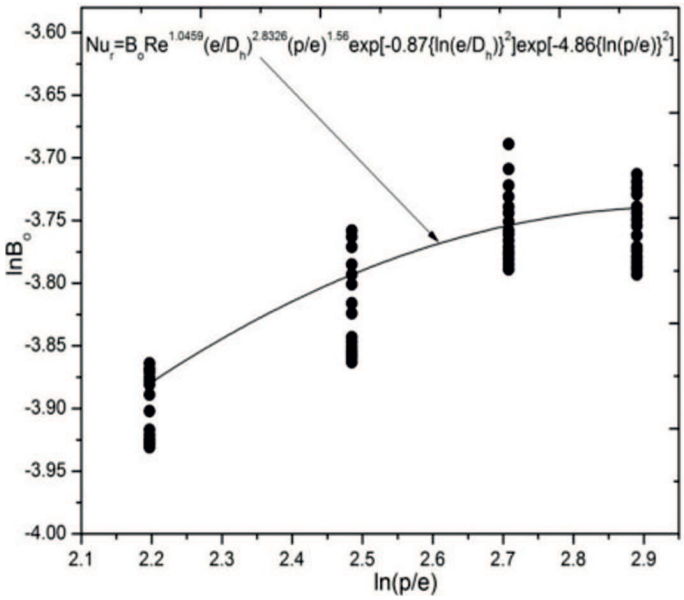

Figure 11: Plot of $\ln B_0$ *vs.* $\ln(p/e)$.

Finally, the plot for $\ln B_0$ *versus* $\ln(p/e)$ is presented in Fig. 12. Finally, a 2nd order quadratic curve fit in following form is obtained

$$\ln\left[\frac{\mathrm{Nu}}{\mathrm{Re}^{1.0459}} \left(\frac{e}{D_h}\right)^{2.8326} \exp\left(-0.87\right) \left(\ln\frac{e}{D_h}\right)^2\right] = \ln B_0 + B_1 \ln\frac{p}{e} + B_2 \left(\ln\frac{p}{e}\right)^2. \tag{18}$$

Substituting the values of slopes and intercepts obtained, Eq. (18) can be

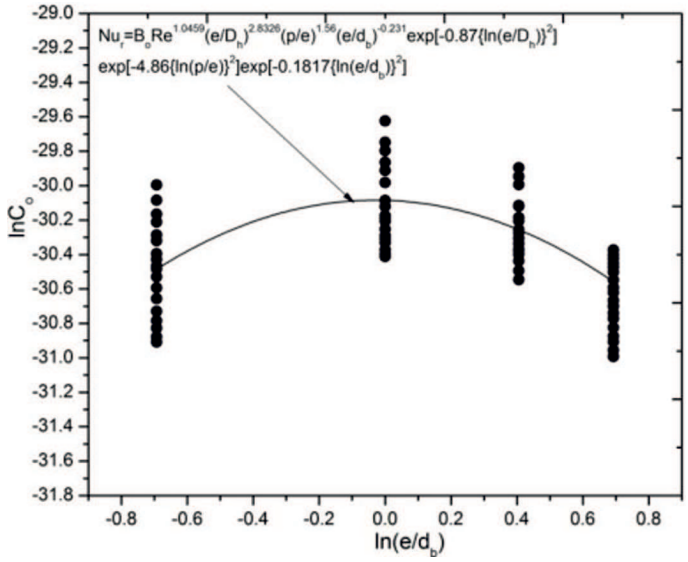

Figure 12: Plot of $\ln C_0$ *vs.* $\ln(e/d_b)$.

rewritten as

$$\frac{\mathrm{Nu}}{\mathrm{Re}^{1.0459}}\left(\frac{e}{D_h}\right)^{2.8326}\exp\left(-0.87\right)\left(\ln\frac{e}{D_h}\right)^2 = B_0\left(\frac{p}{e}\right)^{1.56}\exp\left(-4.86\right)\left(\ln\frac{p}{e}\right)^2. \tag{19}$$

The constant C_o will be a function of other roughness parameter, i.e., e/d_b. To visualize the effect of e/d_b, the expression

$$\frac{\mathrm{Nu}}{\mathrm{Re}^{1.0459}}\left(\frac{e}{D_h}\right)^{2.8326}\left(\frac{p}{e}\right)^{1.56}\exp\left(-0.87\right)\left(\ln\frac{e}{D_h}\right)^2\exp\left(-4.86\right)\left(\ln\frac{p}{e}\right)^2$$

was found using experimental Nu_r obtained at constant p/e, e/D_h, and α values. These values are plotted against respective e/d_b values as depicted in Fig. 12.

Expression for the constant B_o can be written as

$$B_0 = \frac{\frac{\mathrm{Nu}}{\mathrm{Re}^{1.0459}}}{\left(\frac{e}{D_h}\right)^{2.8326}\left(\frac{p}{e}\right)^{1.56}\exp\left(-0.87\right)\left(\ln\frac{e}{D_h}\right)^2\exp\left(-4.86\right)\left(\ln\frac{p}{e}\right)^2}. \tag{20}$$

Finally, the plot for $\ln C_0$ versus depth to diameter ratio e/d_b was drawn as depicted in Fig. 12. Hence, a 2nd order quadratic curve fit in the following form is obtained:

$$\ln\left[\frac{\mathrm{Nu}}{\mathrm{Re}^{1.0459}}\left(\frac{e}{D_h}\right)^{2.8326}\exp(-0.87)\left(\ln\frac{e}{D_h}\right)^2\left(\frac{p}{e}\right)^{1.56} \times \exp(-4.86)\left(\ln\frac{p}{e}\right)^2\right] = \ln C_0 + C_1\ln\left(\frac{e}{d_b}\right) + C_2\left(\ln\frac{p}{e}\right)^2. \quad (21)$$

Substituting the values of slopes and intercepts obtained, Eq. (21) can be rewritten as

$$\frac{\mathrm{Nu}}{\mathrm{Re}^{1.0459}}\left(\frac{e}{D_h}\right)^{2.8326}\left(\frac{p}{e}\right)^{1.56}\exp(-0.87)\left(\ln\frac{e}{D_h}\right)^2 \times \exp(-4.86)\left(\ln\frac{p}{e}\right)^2 = C_0\left(\frac{e}{d_b}\right)^{-0.231}\exp(-0.1817)\left(\ln\frac{e}{d_b}\right)^2. \quad (22)$$

The constant C_0 will be a function of other roughness parameter, i.e., $\alpha/55$. To visualize the effect of $\alpha/55$, the expression

$$\frac{\mathrm{Nu}}{\mathrm{Re}^{1.0459}}\left(\frac{e}{D_h}\right)^{2.8326}\left(\frac{p}{e}\right)^{1.56}\left(\frac{e}{d_b}\right)^{-0.231}\exp(-0.87)\left(\ln\frac{e}{D_h}\right)^2 \times \exp(-4.86)\left(\ln\frac{p}{e}\right)^2\exp(-0.1817)\left(\ln\frac{e}{d_b}\right)^2,$$

was determined using experimental Nu_r obtained at constant p/e, e/D_h, and e/d_b. These values are plotted against respective $\alpha/55$ values as depicted in Fig. 13.

Expression for the constant C_o can be written as

$$C_0 = \frac{\mathrm{Nu}}{\mathrm{Re}^{1.0459}}\left[\left(\frac{e}{D_h}\right)^{2.8326}\left(\frac{p}{e}\right)^{1.56}\left(\frac{e}{d_b}\right)^{-0.231}\exp(-0.87)\left(\ln\frac{e}{D_h}\right)^2 \times \exp(-4.86)\left(\ln\frac{p}{e}\right)^2\exp(-0.1817)\left(\ln\frac{e}{d_b}\right)^2\right]^{-1}. \quad (23)$$

Finally, the plot for $\ln D_o$ versus depth to diameter ratio $\alpha/55$ was drawn as depicted in Fig. 13. Hence, a 2nd order quadratic curve fit in the following

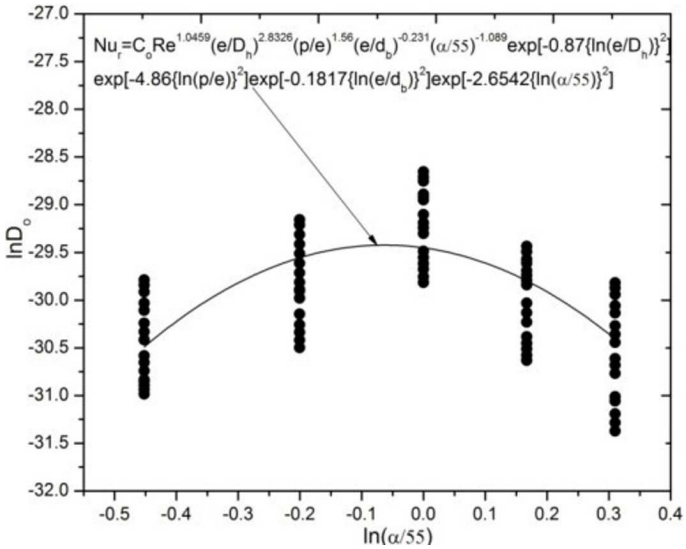

Figure 13: Plot of $\ln D_0$ *vs.* $\ln(\alpha/55)$.

form is obtained:

$$\ln\left[\frac{\mathrm{Nu}}{\mathrm{Re}^{1.0459}}\left(\frac{e}{D_h}\right)^{2.8326}\left(\frac{p}{e}\right)^{1.56}\left(\frac{e}{d_b}\right)^{-0.231}\exp\left(-0.87\right)\left(\ln\frac{e}{D_h}\right)^2 \times \exp\left(-4.86\right)\left(\ln\frac{p}{e}\right)^2\exp\left(-0.1817\right)\left(\ln\frac{e}{d_b}\right)^2\right] = \ln D_0 + D_1\ln\alpha + D_2\left(\ln\frac{\alpha}{55}\right)^2 . \tag{24}$$

Substituting the values of slopes and intercepts obtained, Eq. (24) can be rewritten as

$$\frac{\mathrm{Nu}}{\mathrm{Re}^{1.0459}}\left(\frac{e}{D_h}\right)^{2.8326}\left(\frac{p}{e}\right)^{1.56}\left(\frac{e}{d_b}\right)^{-0.231}\exp\left(-0.87\right)\left(\ln\frac{e}{D_h}\right)^2 \times \exp\left(-4.86\right)\left(\ln\frac{p}{e}\right)^2\exp\left(-0.1817\right)\left(\ln\frac{e}{d_b}\right)^2 = D_0\left(\frac{\alpha}{55}\right)^{-1.089}\exp\left(-2.6542\right)\left(\ln\frac{\alpha}{55}\right)^2 . \tag{25}$$

The above analysis resulted in the following correlation for the Nu_r:

$$\mathrm{Nu}_r = 5.8 \times 10^{-7} \mathrm{Re}^{1.0459} \left(\frac{e}{D_h}\right)^{2.8326} \left(\frac{p}{e}\right)^{1.56} \left(\frac{e}{d_b}\right)^{-0.231} \left(\frac{\alpha}{55}\right)^{-1.089} \times \exp(-0.87) \left(\ln\frac{e}{D_h}\right)^2 \exp(-4.86) \left(\ln\frac{p}{e}\right)^2 \exp(-0.1817) \left(\ln\frac{e}{d_b}\right)^2 \times \exp(-2.6542) \left(\ln\frac{\alpha}{55}\right)^{-2}. \quad (26)$$

3.3 Friction factor correlation

Friction factor depended strongly upon roughness geometry and flow parameters. The effect of these roughness parameters namely: e/D_h, p/e, e/d_b, $\alpha/55$ and the effect of flow parameter, i.e., Re on f_r were discussed in detail. The effects of these parameters on f_r found are given below:

- f_r monotonously decreases with increasing Re,
- f_r monotonously decreases with increase in p/e,
- f_r increases monotonously with increasing e/D_h,
- f_r varies with the variation in depth to diameter ratio (e/d_b) and attains a maxima at $e/d_b = 1$ and minima at $e/d_b = 2$,
- f_r varies with the variation in relative angle of attack ($\alpha/55$) and attains a maxima at $\alpha = 55°$ and minima at $\alpha = 35°$.

Regression analysis was conducted on experimentally collected data to derive statistical correlations for the friction factor. A functional relationship between f_r and Re was obtained by plotting $\ln(f_r)$ and $\ln(\mathrm{Re})$ for all the data points as depicted in Fig. 14.
A regression analysis to obtain the best fit curve through these points is given by

$$f = A_0 \mathrm{Re}^{-0.05629}, \quad (27)$$

where A_0 is a function of other roughness parameters.

To visualize the effects of relative roughness height (e/D_h), the values are computed from the experimental data of friction factor obtained at constant values of other roughness parameters like p/e, e/d_b, and $\alpha/55$. These values have been plotted against respective e/D_h values. Regression

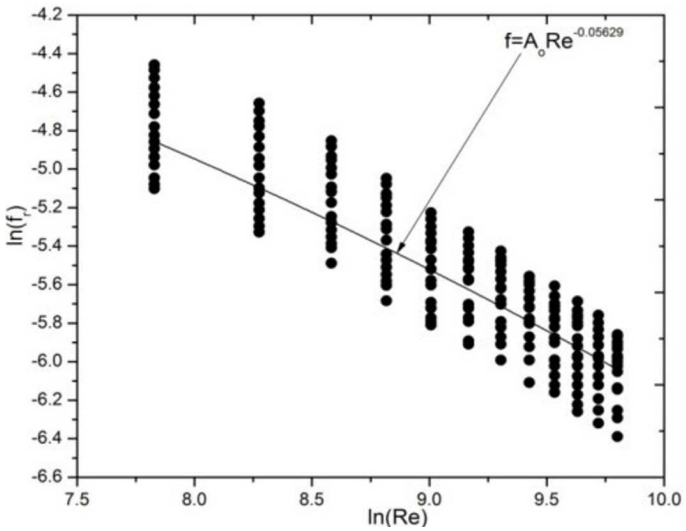

Figure 14: Variation in $\ln f$ with $\ln \mathrm{Re}$.

analysis for fitting 2nd order quadratic curve is represented by following expression:

$$\ln\left(\frac{f}{\mathrm{Re}^{-0.05629}}\right) = \ln A_0 + A_1 \ln\frac{e}{D_h} + A_2\left(\ln\frac{e}{D_h}\right)^2 . \tag{28}$$

From the first order regression of the data, the value of slope (m) is obtained as -0.05629. By putting the value of slope in Eq. (28), a following correlation has been obtained:

$$\frac{f}{\mathrm{Re}^{-0.05629}} = A_0\left(\frac{e}{D_h}\right)^{0.0751} \exp\left(0.0664\right)\left(\ln\frac{e}{D_h}\right)^2 . \tag{29}$$

A plot of $\ln A_o$ *versus* $\ln(e/D_h)$ is shown in Fig. 15. The constant A_o shall be a function of the relative roughness pitch (p/e). To introduce the effect of p/e, the values of the expression

$$\frac{f}{\mathrm{Re}^{-0.05629}}\left(\frac{e}{D_h}\right)^{0.0751} \exp\left(0.0664\right)\left(\ln\frac{e}{D_h}\right)^2 ,$$

have been computed from experimental data of friction factor obtained at constant e/D_h, e/d_b, and $\alpha/55$. These values are plotted against respective p/e values as depicted in Fig. 16.

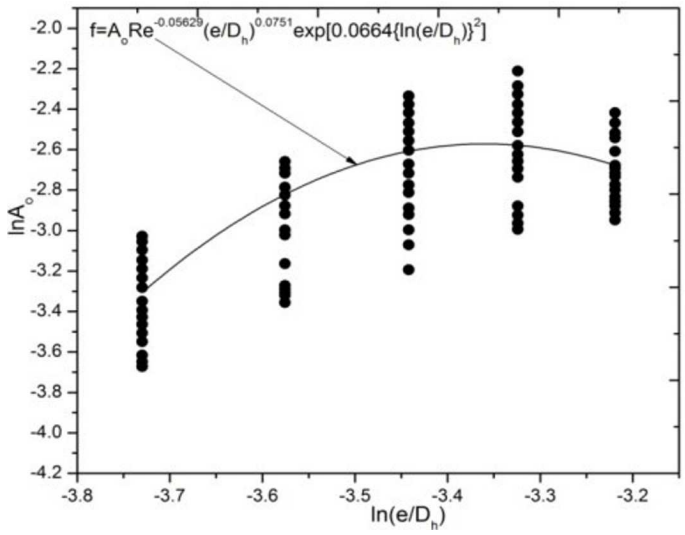

Figure 15: Plot of $\ln A_0$ *vs.* $\ln(e/D_h)$.

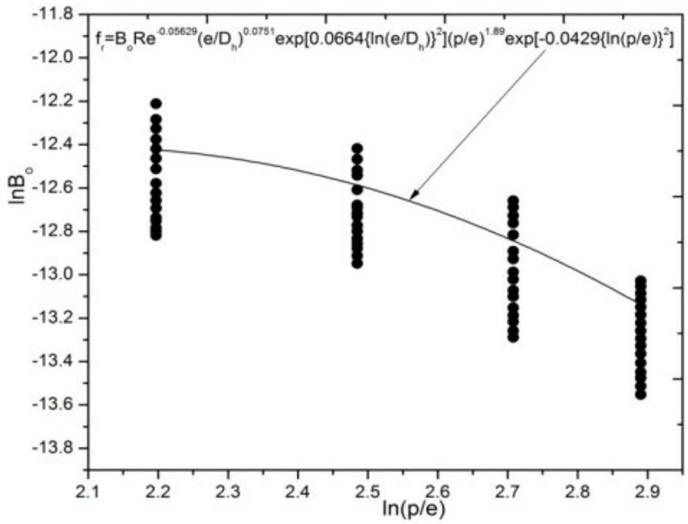

Figure 16: Plot of $\ln B_o$ *vs.* $\ln(p/e)$.

Expression for the constant B_o can be written as

$$B_0 = \frac{\frac{f}{\mathrm{Re}^{-0.05629}}}{\left(\frac{e}{D_h}\right)^{0.0751} \exp\left(0.0664\right) \left(\ln \frac{e}{D_h}\right)^2}. \tag{30}$$

Finally, the plot for $\ln B_0$ *versus.* $\ln(p/e)$ is presented in Fig. 16. A 2nd order quadratic curve fit in the following form is obtained:

$$\ln\left[\frac{f}{\mathrm{Re}^{-0.05629}}\left(\frac{e}{D_h}\right)^{0.0751}\exp\left(0.0664\right)\left(\ln\frac{e}{D_h}\right)^2\right] = \ln B_0 + B_1\ln\frac{p}{e} + B_2\left(\ln\frac{p}{e}\right)^2. \tag{31}$$

Substituting the values of slopes and intercepts obtained, Eq. (31) can be rewritten as

$$\frac{f}{\mathrm{Re}^{-0.05629}}\left(\frac{e}{D_h}\right)^{0.0751}\exp\left(0.0664\right)\left(\ln\frac{e}{D_h}\right)^2 = B_0\left(\frac{p}{e}\right)^{1.89}\exp\left(-0.0429\right)\left(\ln\frac{p}{e}\right)^2. \tag{32}$$

The constant B_o will be a function of the spherical ball height to diameter ratio (e/d_b). To observe the effect of e/d_b, the values of the expression

$$\frac{f}{\mathrm{Re}^{-0.05629}}\left(\frac{e}{D_h}\right)^{0.0751}\left(\frac{p}{e}\right)^{1.89}\exp\left(0.0664\right)\left(\ln\frac{e}{D_h}\right)^2\exp\left(-0.0429\right)\left(\ln\frac{p}{e}\right)^2$$

have been computed from experimental data of friction factor obtained at constant values of e/D_h, p/e, and $\alpha/55$. These values are plotted against respective e/d_b values as depicted in Fig. 17.

Expression for the constant C_o can be written as

$$C_0 = \frac{\frac{f}{\mathrm{Re}^{-0.05629}}}{\left(\frac{e}{D_h}\right)^{0.0751}\left(\frac{p}{e}\right)^{1.89}\exp\left(0.0664\right)\left(\ln\frac{e}{D_h}\right)^2\exp\left(-0.0429\right)\left(\ln\frac{p}{e}\right)^2}. \tag{33}$$

Finally, the plot for $\ln C_o$ *versus* $\ln(e/d_b)$ is presented in Fig. 17. A 2nd order quadratic curve fit in following form is obtained:

$$\ln\left[\frac{f}{\mathrm{Re}^{-0.05629}}\left(\frac{e}{D_h}\right)^{0.0751}\exp\left(0.0664\right)\left(\ln\frac{e}{D_h}\right)^2\left(\frac{p}{e}\right)^{1.89} \times \exp\left(-0.0429\right)\left(\ln\frac{p}{e}\right)^2\right] = \ln C_0 + C_1\ln\frac{e}{d_b} + C_2\left(\ln\frac{e}{d_b}\right)^2, \tag{34}$$

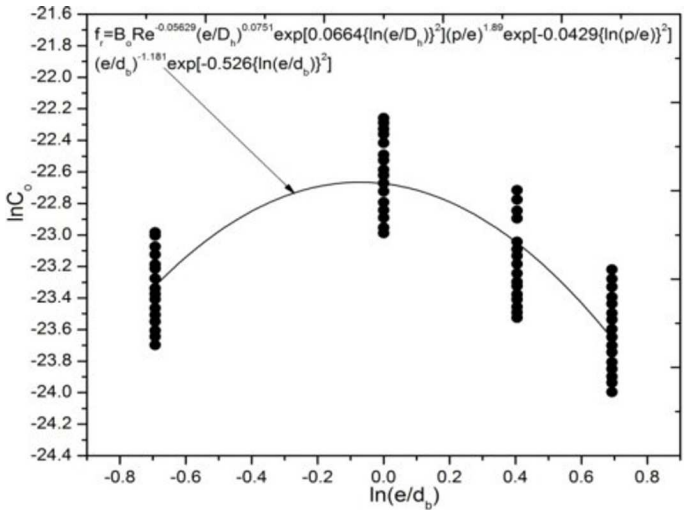

Figure 17: Plot of $\ln C_0$ *vs.* $\ln(e/d_b)$.

Substituting the values of slopes and intercepts obtained, Eq. (34) can be rewritten as

$$\frac{f}{\mathrm{Re}^{-0.05629}}\left(\frac{e}{D_h}\right)^{0.0751}\exp\left(0.0664\right)\left(\ln\frac{e}{D_h}\right)^2\left(\frac{p}{e}\right)^{1.89} \times \exp\left(-0.0429\right)\left(\ln\frac{p}{e}\right)^2 = D_0\left(\frac{e}{d}\right)^{-1.181}\exp\left(-0.526\right)\left(\ln\frac{e}{d_b}\right)^2 . \quad (35)$$

The constant D_o will be a function of the relative angle of attack $(\alpha/55)$. To observe the effect of $\alpha/55$, the values of the expresion

$$\frac{f}{\mathrm{Re}^{-0.05629}}\left(\frac{e}{D_h}\right)^{0.0751}\left(\frac{p}{e}\right)^{1.89}\exp\left(0.0664\right)\left(\ln\frac{e}{D_h}\right)^2\exp\left(-0.0429\right)\left(\ln\frac{p}{e}\right)^2$$

have been computed from experimental data of friction factor obtained at constant values of e/D_h, p/e, and e/d_b. These values are plotted against respective $\alpha/55$ values as depicted in Fig. 18.

Expression for the constant D_o can be written as

$$D_o = \frac{f}{\mathrm{Re}^{-0.05629}}\left[\left(\frac{e}{D_h}\right)^{0.0751}\left(\frac{p}{e}\right)^{1.89}\left(\frac{\alpha}{55}\right)^{-0.1127}\exp\left(0.0664\right)\left(\ln\frac{e}{D_h}\right)^2 \times \exp\left(-0.0429\right)\left(\ln\frac{p}{e}\right)^2\exp\left(-2.352\right)\left(\ln\frac{\alpha}{55}\right)^2\right]^{-1} . \quad (36)$$

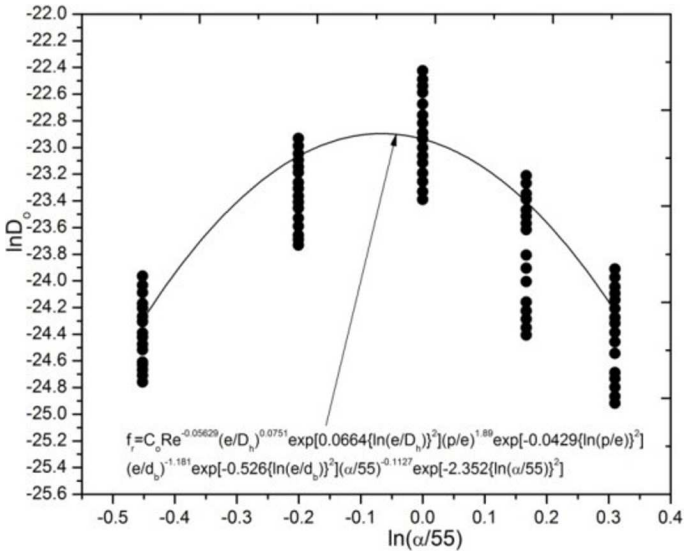

Figure 18: Plot of $\ln D_o$ *vs.* $\ln(\alpha/55)$.

Finally, the plot for $\ln D_o$ *versus* $\ln(\alpha/55)$ is presented in Fig. 18. A 2nd order quadratic curve fit in the following form is obtained:

$$\ln\left[\frac{f}{\mathrm{Re}^{-0.05629}}\left(\frac{e}{D_h}\right)^{0.0751}\exp(0.0664)\left(\ln\frac{e}{D_h}\right)^2\right]\left(\frac{p}{e}\right)^{1.89} \times\left[\exp(-0.0429)\left(\ln\frac{p}{e}\right)^2\left(\frac{\alpha}{55}\right)^{-0.1127}\exp(-2.352)\left(\ln\frac{\alpha}{55}\right)^2\right] = \ln D_0 + D_1\ln\frac{\alpha}{55} + D_2\left(\ln\frac{\alpha}{55}\right)^2. \tag{37}$$

Substituting the values of slopes and intercepts obtained, Eq. (37) can be rewritten as

$$\frac{f}{\mathrm{Re}^{-0.05629}}\left(\frac{e}{D_h}\right)^{0.0751}\exp(0.0664)\left(\ln\frac{e}{D_h}\right)^2\left(\frac{p}{e}\right)^{1.89} \times\exp(-0.0429)\left(\ln\frac{p}{e}\right)^2\left(\frac{e}{d}\right)^{-1.181}\exp(-0.526)\left(\ln\frac{e}{d_b}\right)^2 = D_0\left(\frac{\alpha}{55}\right)^{-0.1127}\exp(-2.352)\left(\ln\frac{\alpha}{55}\right)^2. \tag{38}$$

The above analysis resulted in the following correlation for the friction

factor:

$$f_r = 2.38\mathrm{Re}^{-0.05629}\left(\frac{e}{D_h}\right)^{0.0751}\left(\frac{p}{e}\right)^{1.89}\left(\frac{e}{d}\right)^{-1.181}\left(\frac{\alpha}{55}\right)^{-0.1127} \times \exp(0.0664)\left(\ln\frac{e}{D_h}\right)^2 \exp(-0.0429)\left(\ln\frac{p}{e}\right)^2 \exp(-0.526) \times \left(\ln\frac{e}{d_b}\right)^2 \exp(-2.352)\left(\ln\frac{\alpha}{55}\right)^2 . \quad (39)$$

3.4 Comparison of experimental and predicted values of Nusselt number and friction factor

Figure 19 shows the difference between experimental data of the Nusselt number (Nu_r) and calculated using correlation developed in Eq. (26). A good agreement can be observed. The average absolute percentage deviation between experimental and calculated Nu_r was 8.61%, while 91% data points lie within ± 10.5%. Figure 20 presents the comparison between experimental and calculated values of the friction factor (f_r) using a correlation derived in Eq. (39). Average absolute percentage deviation between experimental and calculated values for f_r was found as 4.21%, while the 95% data points lie within ±9.5%.

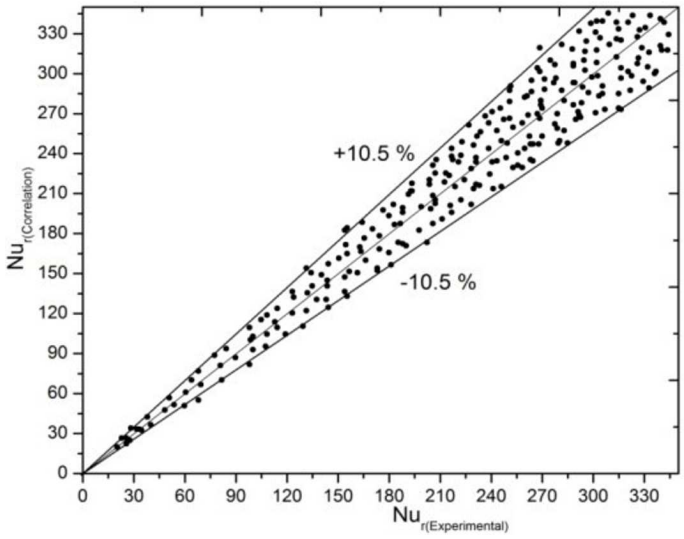

Figure 19: Comparison between calculated and experimental values of Nu_r.

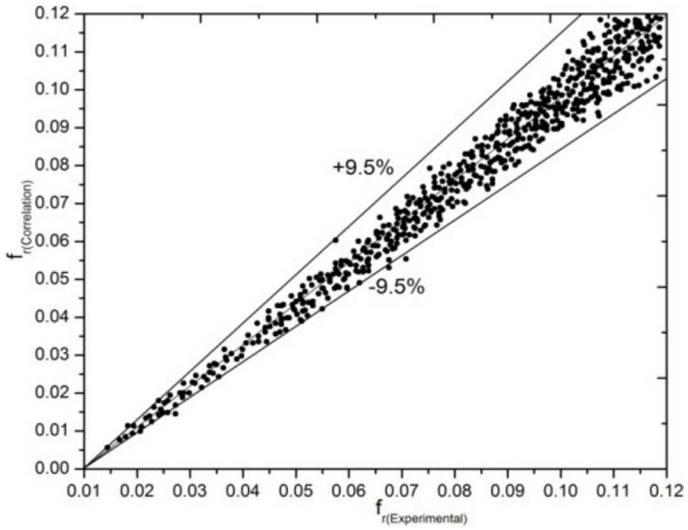

Figure 20: Comparison between calculated and experimental values of f_r.

An elaborative experimental investigations have been carried out under actual outdoor conditions to test the inclined spherical ball roughened solar air heater (SAH) and parametric impact on heat transfer and friction characteristics. Nusselt number increased with an increase in Reynolds number but friction factor decreased. At higher flow rate, more heat transfer from absorber to air is obtained as the primary and secondary flow both heats the air. Power required to propel air through roughened ducts is increased at higher flow rate that reduces the overall performance of the collector. Hence, present study establishes a balance between the rise in Nusselt number and friction factor in terms of roughness and flow parameters, as experimental data have been used to derive a statistical correlation for the Nusselt number ($\mathrm{Nu}_{r)}$ and friction factor for roughened duct (f_r) in terms of variable parameters. The following conclusions can be drawn from the present study:

- Nu_r and f_r varied as p/e, e/D_h, e/d_b, and $\alpha/55$ were varied under the given operating range. In the entire range of Reynolds number studied, Nu_r increased as p/e was increased from 9 to 15. On further increasing the value of p/e, Nu_r decreased.

- A similar trend has been found in Nu_r with the variation in e/D_h. Nu_r increased as the e/D_h was increased from 0.024 to 0.036, beyond

this, Nusselt number decreased with increase in e/D_h value.

- An increase in ball height to diameter ratio e/d_b resulted in an increase in Nu_r from 0.5 to 1. Upon increasing e/d_b from 1 to 2, it was found Nu_r value was less than so obtained at e/d value of 1.

- Angle of attack $\alpha/55$ affected the heat transfer rise as the value of Nu_r increased as angle of attack was increased from 35° to 55°. On further increament in angle of attack value, the Nu_r started decreasing such that the maximum and minimum value of Nu_r was obtained at an angle of attack of 55° and 75°, respectively.

- The enhancement in Nu_r was found to be strongly associated with roughness and flow parameters. The maximum augmentation in Nu_r for varying p/e, $e/D_h, e/d_b$, and $\alpha/55$ was respectively found to be of the order of 2.1 to 3.54 times, 1.87 to 3.21 times, 2.89 to 3.27 and 1.74 to 3.56 times compared to non-roughened duct. The optimum roughness parameters found under present investigation is $p/e = 15$, $e/D_h = 0.036$, $e/d_b = 1$ and $\alpha = 55°$.

- Augmentation in Nu_r is achieved along with friction factor rise across the roughened ducts. Friction has been found to decrease monotonously as the p/e was increased from 9 to 18.

- With the variation of e/D_h from 0.024 to 0.04, the values of f_r increased monotonously with variation in flow and other roughness parameters.

- As e/d_b was varied from 0.5 to 1, the values of friction factor increased and as the e/d_b values were varied from 1 to 2, the values of friction factor decreased for the entire Reynolds number range investigated.

- The f_r increased as the angle of attack (α) was increased from 35° to 55°. For further increament in angle of attack from 55° to 75°, f_r decreased.

- The maximum augmentation in f_r for varying p/e, $e/D_h, e/d_b$, and α was respectively found to be of the order of 0.84 to 1.79 times, 1.46 to 1.91 times, 1.67 to 2.34 times and 1.21 to 2.67 times compared to the non-roughened duct.

- Data for Nu_r and f_r collected from experimentation revealed that these are a very strong function of p/e, e/D_h, e/d_b, $\alpha/55$, and Re. Using these experimental data, the correlations for Nu_r and f_r for spherical ball roughened SAH were developed as function of these parameters. Correlation for Nusselt number is given in Eq. (26) and correlation for friction factor in Eq. (39).

- Experimental data and data predicted from the above correlation are in good agreement. The mean absolute percentage deviation between the experimental and calculated data for Nu has been equal to 8.61%, while 91% data points lie within the range ±10.5%. The mean absolute percentage deviation between experimental and calculated data for f_r has been equal to 4.21%, while the 95% data points lie within ±9.5%.

Received 12 October 2018

References

[1] *Energy and the challenge of sustainability*. United Nations Development Programme and World Energy Council, New York 2000 (accessed 7 Jan. 2017).

[2] Sukhatme S.P.: *Solar Energy Engineering*. Prentice Hall, New Jersey 1986.

[3] Duffie J.A., Beckman W.A.: *Solar Engineering Thermal Processes*. John Wiley, New York 1991.

[4] Garg H.P., Prakash J.P.: *Solar Energy – Fundamentals and Applications*. Tata McGraw-Hill, New Delhi 1997.

[5] Wan K.K., Li D.H., Liu D., Lam J.C.: *Future trends of building heating and cooling loads and energy consumption in different climates*. Build. Environ. **46**(2011), 1, 223–234.

[6] Biondi P., Cicala L., Farina G.: *Performance analysis of solar air heaters of conventional design*. Sol. Energy **41**(1988), 1, 101–107.

[7] Reddy T.A., Gupta C.L.: *Generating application design data for solar air heating systems*. Sol. Energy **25**(1980), 6, 527–530.

[8] Prasad B.N., Saini J.S.: *Effect of artificial roughness on heat transfer and friction factor in a solar air heater*. Sol. Energy **41**(1988), 6, 555–560.

[9] Gilani S.E., Al-Kayiem H.H., Woldemicheal D.E., Gilani S.I.: *Performance enhancement of free convective solar air heater by pin protrusions on the absorber*. Sol. Energy **151**(2017), 1, 173–185.

[10] Layek A., Saini J.S., Solanki S.C.: *Heat transfer coefficient and friction characteristics of rectangular solar air heater duct using rib-grooved artificial roughness*. Int. J. Heat Mass Tran. **50**(2007), 4845–4854.

[11] Gupta A., Sriharsha V., Prabhu S.V., Vedula R.P.: *Local heat transfer distribution in a square channel with 90° continuous, 90° saw tooth profiled and 60° broken ribs.* Exp. Therm. Fluid Sci. **32**(2008), 997–1010.

[12] Han J.C., Park J.S., Lei C.K.: *Heat transfer enhancement in channel with turbulence promoters.* Eng. Gas Turb. Power-T ASME **107**(1985), 3, 628–635.

[13] Saini S.K., Saini R.P.: *Development of correlations for Nusselts number and friction factor for solar air heater with roughened duct having arc-shaped wire as artificial roughness.* Sol. Energy **82**(2008), 1118–1130.

[14] Lau S.C., McMillan R.D., Han J.C.: *Turbulent heat transfer and friction in a square channel with discrete rib tabulators.* J. Heat Trans.-T ASME **113**(1991), 3, 360–366.

[15] Karwa R., Solanki S.C., Saini J.S.: *Heat transfer coefficient and friction factor correlation for the transitional flow regime in rib-roughened rectangular duct.* Int. J. Heat Mass Tran. **42**(1999), 9, 1597–1615.

[16] Chang S.W., Liou T.M., Chiang K.F., Hong G.F.: *Heat transfer and pressure drop in rectangular channel with compound roughness of V-shaped ribs and deepened scales.* Int. J. Heat Mass Tran. **51**(2008), 457–468.

[17] Mahmood G.I., Ligrani P.M., Chen K.: *Variable property and temperature ratio effects on Nusselts number in a rectangular channel with 45° angled rib turbulators.* J. Heat Transf. 125(2003), 769–778.

[18] Ridouane E.I.H., Campo A.: *Heat transfer and pressure drop characteristics of laminar air flows moving in a parallel-plate channel with transverse hemi-cylindrical cavities.* Int. J. Heat Mass Tran. **50**(2007), 3913–3924.

[19] Chandra P.R., Alexander C.R., Han J.C.: *Heat transfer and friction behaviors in rectangular channel with varying number of ribbed walls.* Int. J. Heat Mass Tran. **46**(2003), 481–495, .

[20] Gupta D., Solanki S.C., Saini J.S.: *Thermohydraulic performance of solar air heaters with roughened absorber plates.* Sol. Energy **61**(1997), 33–42.

[21] Gupta D., Solanki S.C., Saini J.S.: *Heat and fluid flow in rectangular solar air heater ducts having transverse rib roughness on absorber plate.* Sol. Energy **51**(1993), 31–37.

[22] Momin A.M.E., Saini J.S., Solanki S.C.: *Heat transfer and friction in solar air heater duct with V-shaped rib roughness on absorber plate.* Int. J. Heat Mass Tran. **45**(2002), 16, 3383–3396 .

[23] Saini R.P., Saini J.S.: *Heat transfer and friction factor correlations for artificially roughened ducts with expanded metal mesh as roughness element.* Int. J. Heat Mass Tran. **40**(1997), 4, 973–986.

[24] Varun Saini R.P., Singal S.K.: *Investigation on thermal performance of solar air heaters having roughness elements as a combination of inclined and transverse ribs on the absorber plate.* Renew. Energy **33**(2008), 1398–1405.

[25] Wongcharee K., Changcharoen, W. Eiamsa-Ard S.: *Numerical investigation of flow friction and heat transfer in a channel with various shaped ribs mounted on two opposite ribbed walls.* Int. J. Chem. Reactor Eng. **9**(2011), 1–21.

[26] Sethi M., Varun Thakur N.S.: *Correlations for solar air heater duct with dimpled shape roughness elements on absorber plate*. Sol. Energy **86**(2012), 2852–61.

[27] Skullong S., Promvonge P.: *Experimental investigation on turbulent convection in solar air heater channel fitted with delta winglet vortex generator*. Chin. J. Chem. Eng. **22**(2014), 1, 1–10.

[28] Pandey N.K., Bajpai V.K., Varun: *Experimental investigation of heat transfer augmentation using multiple arcs with gap on absorber plate of solar air heater*. Sol. Energy **134**(2016), 314–326.

[29] Kumar V., Prasad L.: *Experimental investigation on heat transfer and fluid flow of air flowing under three sides concave dimple roughened duct*. Int. J. Mech. Eng. Technol. (IJMET) **8**(2017), 11, 1083–1094.

[30] Kumar V., Prasad L.: *Thermal performance investigation of one and three sides concave dimple roughened solar air heaters*. Int. J. Mech. Eng. Technol. (IJMET) **8**(2017), 12, 31–45.

[31] Kumar, V., Prasad L.: *Performance Analysis of three sides concave dimple shape roughened solar air heater*. J. Sustain. Dev. Energy Water Environ. Sys. **6**(2018), 4, 631–648.

[32] ASHRAE Standard 93-97: *Methods of testing to determine the thermal performance of solar collectors*. American Society of Heating, Refrigerating and Air-Conditioning Engineers, Atlanta 1977.

[33] Kline S.J., McClintock F.A.: *Describing uncertainties in single sample experiments*. Mech. Eng. **75**(1953), 3–8.